

Review

Tailoring Microstructure of Austenitic Stainless Steel with Improved Performance for Generation-IV Fast Reactor Application: A Review

Shenghu Chen ^{1,*}, Ang Xie ^{1,2}, Xinliang Lv ^{1,2} , Sihan Chen ¹, Chunguang Yan ³, Haichang Jiang ¹ and Lijian Rong ¹

¹ Key Laboratory of Nuclear Materials and Safety Assessment, Institute of Metal Research, Chinese Academy of Sciences, Shenyang 110016, China

² School of Materials Science and Engineering, University of Science and Technology of China, Hefei 230026, China

³ China Institute of Atomic Energy (CIAE), Beijing 102413, China

* Correspondence: chensh@imr.ac.cn; Tel.: +86-24-23971981

Abstract: Austenitic stainless steels are selected as candidate materials for in-core and out-of-core components of Generation-IV fast reactors due to their excellent operating experience in light-water reactors over several decades. However, the performance of conventional austenitic stainless steels proves to be inadequate through operation feedback in fast reactors. To withstand the demands for material performance exposure to the extreme operating environment of fast reactors, modified austenitic stainless steels for in-core and out-of-core components have been developed from the first-generation 300-series steels. The design of an appropriate microstructure becomes a top priority for improving material performance, and key metallurgical features including δ -ferrite content, grain size and secondary phase precipitation pertinent to austenitic stainless steel are focused on in this paper. δ -ferrite content and grain size are closely correlated with the fabrication program and their effects on mechanical properties, especially creep and fatigue properties are critically assessed. Moreover, the impacts of some major elements including nitrogen, stabilization elements (Nb, Ti, V), phosphorus and boron on secondary phase precipitation behaviors during aging or creep are reviewed in detail. Based on the role of the aforementioned metallurgical features, the recommended specification of nitrogen content, stabilization ratio, phosphorus content, boron content, δ -ferrite content and grain size are put forward to guarantee the best-expected performance, which could provide reactors designers with attractive options to optimize fast reactor systems.

Keywords: fast reactor; austenitic stainless steel; improved performance; δ -ferrite; grain size; secondary phase evolution



Citation: Chen, S.; Xie, A.; Lv, X.; Chen, S.; Yan, C.; Jiang, H.; Rong, L. Tailoring Microstructure of Austenitic Stainless Steel with Improved Performance for Generation-IV Fast Reactor Application: A Review. *Crystals* **2023**, *13*, 268. <https://doi.org/10.3390/cryst13020268>

Academic Editor: Shouxun Ji

Received: 13 January 2023

Revised: 30 January 2023

Accepted: 31 January 2023

Published: 3 February 2023



Copyright: © 2023 by the authors. Licensee MDPI, Basel, Switzerland. This article is an open access article distributed under the terms and conditions of the Creative Commons Attribution (CC BY) license (<https://creativecommons.org/licenses/by/4.0/>).

1. Introduction

Generation IV nuclear energy systems are currently being developed to overcome the limitations of currently deployed Generation II and III light water reactors [1–4]. As the identified Generation IV nuclear reactors, fast neutron reactors with a closed fuel cycle not only make efficient utilization of uranium resources but also minimize long-lived radioactive waste, thus establishing a more sustainable nuclear energy system. Sodium, lead, or helium can be selected as the coolant in fast neutron reactors. At present, the most mature technology is the sodium-cooled fast reactor, and most of the basic technology has been established through the long-term experience of design, construction, test, operation, inspection and maintenance of demonstration/prototype reactors in the USA, France, Russia, Japan, India, South Korea and China [5]. Besides, the demonstration activities of lead-cooled fast reactors and gas-cooled fast reactors are underway and planned [6].

Developing advanced structural materials is crucial to the success of fast neutron reactors. The extreme operating environment including higher temperature, higher neutron doses, thermal stress and extremely corrosive environment poses significant challenges to the material selection and qualification efforts [7–10]. Taking into account the example of the sodium-cooled fast reactor, the key challenges imposed on in-core structural materials are to be able to simultaneously bear high temperatures up to 700 °C, high peak neutron doses >100 dpa and sodium exposure. Meanwhile, the major challenges of out-of-core structural materials include high temperatures of ~550 °C, long operating periods of 40–60 years and sodium exposure. Most of the operating conditions found in the sodium-cooled fast reactor are also applicable to lead-cooled fast reactors except for the corrosive environment. Experience feedback is very important for nuclear applications. Advanced structural materials suitable for fast neutron reactors are expected to build on the feedback of Generation II and III light water reactors experiences but require significant improvements in specific properties through continuing R&D activities. Several organizations have issued a series of nuclear codes such as the ASME code, RCC-MRx code and JSME code for nuclear power plants and related components [11–13]. All these codes aim to establish rules of safety governing the design, fabrication and inspection during components construction; meanwhile, new advancements in design and materials are constantly being added to the codes.

Conventional austenitic stainless steels such as AISI 304 and 316 show excellent operating experience in light water reactors over several decades and are selected as candidate materials for in-core and out-of-core components of fast reactors [14–21]. However, the performance of conventional austenitic stainless steel proves to be inadequate during operation. For the in-core components including fuel cladding/wrapper, an increase in the fuel life is needed to assure credibility because the first-generation AISI 316 exhibits considerable swelling when irradiated up to 100–120 dpa [14–17]. For the out-of-core components including vessel, core support structure, piping, pump, intermediate heat exchanger, etc., mechanical properties degradation induced by the microstructural evolution during long-term exposure is detrimental to the reliability during the 40–60 years of the design life [18–21]. In order to deal with these challenges in the materials selection of fast reactors, continuous efforts have been made to develop advanced austenitic stainless steels to offer improved safety margins, material reliability and design flexibility.

This paper reviews the extensive research on the improvement in the performance of conventional austenitic stainless steels and ongoing R&D on new alloy development for fast reactors based on the design of an appropriate microstructure. Key metallurgical features including δ -ferrite, grain size, and secondary phase precipitation pertinent to austenitic stainless steel are focused on.

2. Austenitic Stainless Steels for Fast Reactor Application

Candidate austenitic stainless steels for the in-core and out-of-core components of fast reactors are summarized in Table 1. The chemical composition specifications of advanced austenitic stainless steels are carefully modified based on the conventional grade to meet the high-level requirement of design code for fast reactors. Advanced austenitic stainless steels for out-of-core components are optimized in the following: (i) the content of each element is controlled within narrow limits, (ii) tightening the specification ranges of C and N, (iii) upper limits on impurity elements such as Si, S and P. The composition modifications of advanced austenitic stainless steels for in-core components are listed as follows: (i) higher Ni content and lower Cr content are specified, (ii) controlled content of Si, P and B, (iii) addition of stabilizing elements such as Ti, Nb and V. Besides composition optimization, the microstructure is tailored by hot-work, cold-work, heat treatment, etc.

Table 1. Chemical composition specifications of candidate austenitic stainless steels for in-core and out-of-core components of fast reactors.

	Chemical Composition (wt.%)										
	Type	C	N	Ni	Cr	Mn	Mo	Si	Nb	Ti	Others
Conventional Austenitic stainless steels	304	≤0.08	≤0.1	8.0–10.5	18.0–20.0	≤2.0	–	≤0.75	–	–	–
	304L	≤0.03	≤0.1	8.0–10.5	18.0–20.0	≤2.0	–	≤0.75	–	–	–
	316	≤0.08	≤0.1	10.0–14.0	16.0–18.0	≤2.0	2.0–3.0	≤0.75	–	–	–
	316L	≤0.03	≤0.1	10.0–14.0	16.0–18.0	≤2.0	2.0–3.0	≤0.75	–	–	–
Advanced austenitic stainless steels for out-of-core components	Type 304	0.04–0.06	0.04–0.07	8.0–10.0	18.5–20.0	1.0–2.0	≤0.2	≤0.6	–	–	–
	Type 316	0.04–0.06	0.04–0.07	11.0–12.5	17.0–18.0	1.0–2.0	2.5–3.0	≤0.6	–	–	B:0.003
	316FR	≤0.02	0.06–0.12	10.0–14.0	16.0–18.0	≤2.0	2.0–3.0	≤1.0	–	–	B:0.001
	316L(N)	≤0.03	0.06–0.08	12.0–12.5	17.0–18.0	1.6–2.0	2.3–2.7	≤0.5	–	–	B:0.002
	316KD	0.04–0.05	0.05–0.07	11.0–12.5	17.0–18.0	1.0–2.0	2.5–2.7	≤0.6	–	–	–
NF709	≤0.10	0.1–0.25	23.0–26.0	19.5–23.0	≤1.5	1.0–2.0	≤1.0	0.1–0.4	≤0.2	B:0.002	
Advanced austenitic stainless steels for in-core components	PNC316	0.06	–	14.0	16.0	1.8	2.5	0.8	0.08	0.1	B:0.004
	316Ti	0.05	–	14.0	16.0	1.7	2.5	0.6	–	0.4	–
	15/15Ti (1.4970)	0.1	–	15.0	15.0	1.6	1.3	0.5	–	0.5	B:0.003
	D9	0.05	–	15.0	14.0	2.0	2.3	0.6	–	0.25	–
	ChS68	0.05–0.08	–	14.0–15.5	15.5–17.0	1.3–2.0	1.9–2.5	0.3–0.6	–	0.2–0.5	B:0.003
	FV548	0.1	–	11.5	16.5	1.2	1.5	0.35	0.7	–	–
HT-UPS	0.08	–	16.0	14.0	2.0	2.5	0.4	0.1	0.3	B:0.003	

3. δ -Ferrite Formation

Fe-15Cr-15Ni-2Mo model austenitic stainless steels for in-core components such as 15/15Ti, D9 and ChS68 are devoid of δ -ferrite due to a relatively higher Ni_{eq}/Cr_{eq} ratio according to the modified Schaeffler diagram [22–24]:

$$Ni_{eq} = Ni + 21Cr + 11.5N + 0.5Mn \quad (1)$$

$$Cr_{eq} = Cr + 2Mo + 3Si \quad (2)$$

However, austenitic stainless steels for out-of-core components such as Type 316, 316L(N) and 316KD present a higher content of ferrite stabilizing elements such as Cr and Mo to ensure high-temperature properties, resulting in a higher propensity for δ -ferrite formation. Furthermore, the formation of δ -ferrite is promoted in the large-scale billets due to the obvious changes in solidification time and cooling rate across the thickness [25–27]. In the 180 mm thick 316KD continuous casting slab for the Chinese CFR600 demonstration fast reactor [28], different amounts of δ -ferrite are observed across the slab thickness, manifesting as cellular δ -ferrite less than 3% at the surface position and skeletal δ -ferrite up to 8% at the center position (Figure 1). It is found that the combined effects of macro-segregation and cooling rate are responsible for the significant differences in morphologies and amount of δ -ferrite across the thickness, i.e., macro-segregation of Cr, Mo and Ni across thickness alters the Ni_{eq}/Cr_{eq} ratio and a lower cooling rate at the center position increases the time for the solidification reaction.

In light water reactors at the service temperature <350 °C, spinodal decomposition and G phase precipitation are observed within δ -ferrite; cast austenitic stainless steels CF-8 with δ -ferrite contents <20% are less likely to undergo significant thermal embrittlement over the extended lifetimes of reactors (80 years) [29–31]. Upon exposure to the operation temperature of ~550 °C in a fast reactor, δ -ferrite is susceptible to thermal embrittlement through precipitations of $M_{23}C_6$ carbides, Laves phase, σ phase and χ phase, evidenced by a significant reduction in the tensile ductility, impact toughness, creep-rupture strength and fatigue crack growth rate [32–35]. It is reported that the rate of phase precipitation in ferrite is about 100 times more rapid than that in austenite [36]. The δ -ferrite content must be controlled or even limited to have a stable microstructure at high temperatures. For instance, the measured ferrite content of solution-treated X2CrNiMo17-12-2[316L(N)] prod-

ucts including plate, rolled bars, forged bars and forgings must be less than 1% according to the RCC-MRx code [22]. δ -ferrite can be nearly eliminated through δ -ferrite \rightarrow austenite transformation after long-time homogenization treatment at a temperature above 1200 °C (Figure 2), and the elimination of δ -ferrite is mainly a Cr-diffusion controlled process [37]. However, abnormal grain growth occurs during the homogenization treatment, which is not beneficial to obtain uniform grain structure in subsequent hot working and heat treatment.

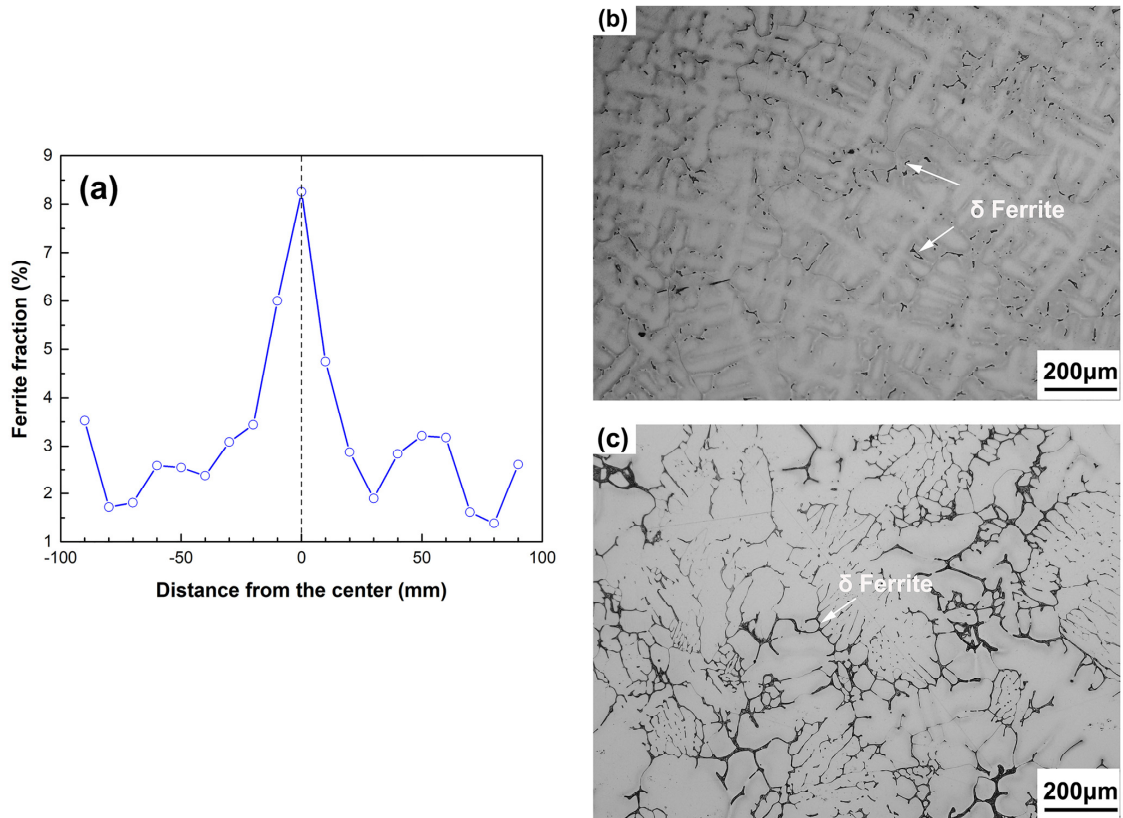


Figure 1. Distribution of δ -ferrite across the slab of 180 mm thick 316KD austenitic stainless steel: (a) area fraction; (b,c) OM images at the surface and center position [28].

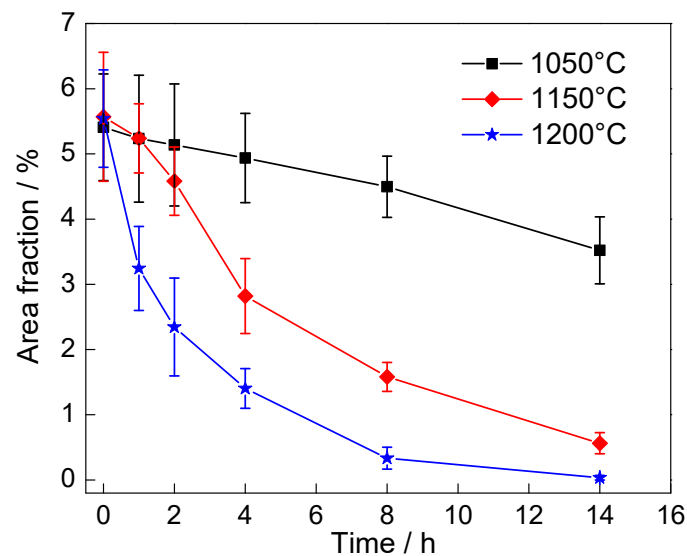


Figure 2. Area fraction of δ -ferrite as a function of homogenization temperature and time of as-cast samples at the center position of 180 mm thick 316KD austenitic stainless steel [37].

4. Grain Size Distribution

Grain size has a profound effect on the mechanical response of metals, and the Hall–Petch relations can provide a reference for understanding the grain size dependence of mechanical strength [38–46]. In order to avoid scatter in mechanical properties, the grain structure is controlled within specific regions besides the narrow limits on chemical composition in the nuclear codes proposed by several organizations. For instance, the grain size number shall be no less than 2 for solution-treated X2CrNiMo17-12-2[316L(N)] products including plate, rolled bars, forged bars and forgings in accordance with RCC-MRx code [22]. The grain size number must be in the range of 3–6 for Type 304 and Type 316 steel in accordance with the ASME-NH code [11]. As the operating temperature reaches ~550 °C in fast reactors, creep and fatigue properties are of great importance to the design and safety evaluation due to the occurrence of creep damage and fatigue damage caused by elevated temperature and thermal stress, apart from conventional tensile strength and impact toughness.

The creep properties of 316FR, 316L(N) and SUS316 at 550 °C and 600 °C show that the creep rupture strength decreases with increasing grain size [41–43]. However, grain size effects are not in agreement with the model by simply incorporating the Hall–Petch relationship into the classical thermally-activated flow model [41]. On the one hand, grain boundary strengthening is moderated at the test temperature because of the occurrence of grain boundary sliding, the recovery process, etc. On the other hand, this is influenced by phase precipitation on moving dislocations during the creep test. Therefore, the grain size effect on the creep properties is a balance between grain boundary strengthening and the strengthening effect by phase precipitation. It is found that the steady-state creep rate decreases to a minimum value at an intermediate grain size (80–130 µm) and then increases with a further increase in the grain size at 600 °C in 316L(N) (Figure 3) [43]. The grain size effect on the steady-state creep rate agrees well with Garofalo’s model on the assumption that grain boundaries act simultaneously as a dislocation source and barriers to dislocation movement. As the test temperature increases further to 700 °C, subgrain structures are developed during the creep deformation, and the size of the resultant subgrains is not related to the initial grain size. Therefore, the creep properties are not significantly influenced by the grain size variation at 700 °C [41].

The effect of grain size on fatigue properties depends on the test temperature, strain range, strain rate and wave shape, so it is difficult to obtain a definitive correlation between the grain size and fatigue resistance as evidenced by the large amount of scatter in the number of cycles to failure (N_f) [44]. When the low-cycle fatigue tests are conducted at a high strain rate ($6.7 \times 10^{-3} \text{ s}^{-1}$) at 600–700 °C of Type 304 and 316, the transgranular fracture mode is observed and N_f scarcely depends on the grain size. As the strain rate decreases to $6.7 \times 10^{-5} \text{ s}^{-1}$, the fracture modes change from transgranular to intergranular, and N_f decreases with an increase in the grain size. The creep-fatigue properties of SUS316 and 316FR at 550 °C reveal that the creep-fatigue life is reduced with increasing grain size [42]. Besides, the creep-fatigue properties of 316H containing a bimodal grain structure with the largest grains larger than 200 µm at 650 °C show that large grains tend to be detrimental to the creep-fatigue life [45]. Metallography from the gauge section reveals that microcracks appear to initiate at the grain boundaries of one of these larger grains.

Until now, the creep and fatigue data as a function of grain size are not sufficient to establish definitive relationships. The available data show that an intermediate grain size can lead to excellent creep resistance and fatigue life. Very large grains are detrimental, which is not acceptable in the microstructure. Besides, grain boundaries are traditionally considered sinks for radiation-induced point defects, but the combination of radiation-induced grain boundary migration and evolving defect sink efficiency makes it difficult to predict the contribution of grain boundaries to radiation resistance through recent investigations [46]. The grain structures are generally determined as a result of material processing history based on the combination of the amount of deformation during hot

working and the subsequent solution treatment [47–50]. Therefore, the processing program of large industrial-scale heat must be carefully selected to avoid extremely large grains.

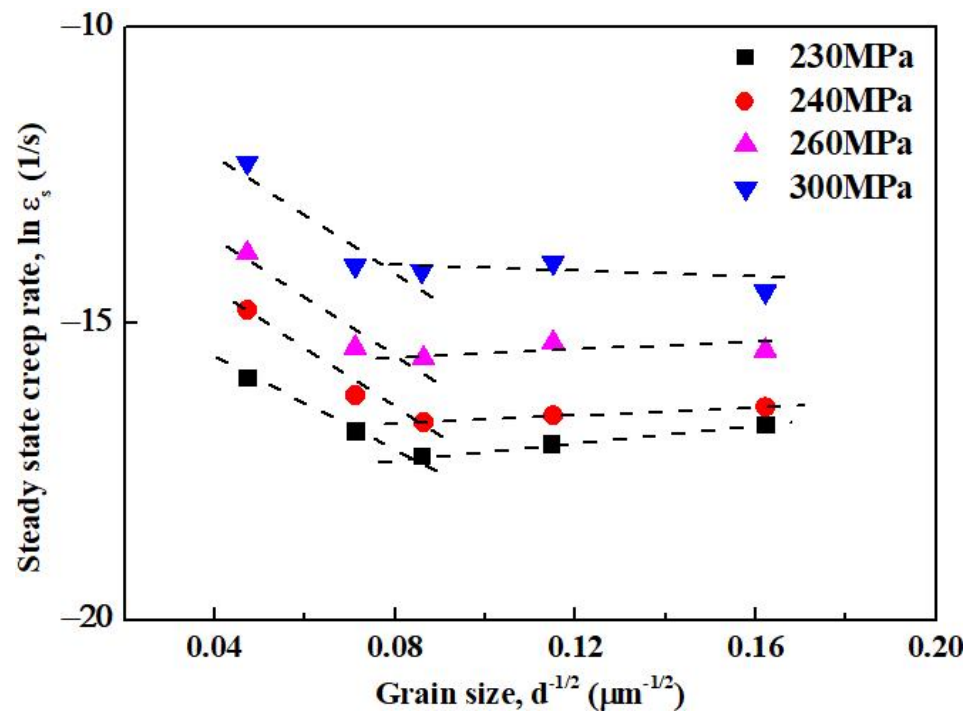


Figure 3. Variation of steady-state creep at various grain sizes after constant load creep test at 600 °C in the range of 230–300 MPa in 316LN austenitic stainless steel. Reproduced from Lee, Y.S.; et al. [43].

5. Secondary Phase Precipitation Behavior

5.1. Secondary Phase Evolution

For austenitic stainless steel products including plate, rolled bars, forged bars and forgings, the final heat treatment before practical use is often solution annealing treatment. The resultant microstructure consists of an austenite matrix with a large number of annealing twins. Long-term exposure to high temperatures in fast reactors can lead to the precipitation of secondary phases, giving rise to a substantial reduction in performance. Besides, radiation-induced solute segregation around point-defect sinks can promote secondary precipitation in these micro-regions. Under neutron irradiation at high temperatures ($>0.3 T_m$, T_m is the absolute melting temperature) in fast reactors, defects with sufficiently high mobilities can rapidly diffuse towards point-defect sinks, and some solute-atoms (such as Ni and Si) strongly coupled to point-defect flows, migrate with them to promote buildups of solute-atoms at these sinks. The most obvious radiation-induced phase is Ni_3Si , which would not form during thermal aging. The radiation-induced solute segregation effects tend to diminish with increasing irradiation temperature, and nearly vanish above 650 °C. Thus, secondary phase evolution is mainly dominated by thermal aging effects in fast reactors.

The time-temperature-precipitation (TTP) diagrams are used to characterize the precipitation sequences of secondary phases and the competition among various phases. TTP diagrams of AISI 316, 316L and 316L(N) have been determined [19], and the typical one of 316L is shown in Figure 4. M_{23}C_6 carbides are the first phase that forms during aging in the range of 500–900 °C. The preferential sites for M_{23}C_6 carbide precipitation are grain boundaries, followed by twin boundaries, and finally within grains. The precipitation of intermetallic phases takes place subsequent to M_{23}C_6 carbides, and the most frequent intermetallic phases are the sigma phase (σ), chi phase (χ) and Laves phase (η). The crystal structures and composition of various phases have been extensively reviewed [36,51,52].

The very slow kinetics of the intermetallic phase precipitation is due to the low diffusivities of the substitutional elements for phase formation and the unfavorable orientation relationship between these phases and the austenite matrix. χ and η show more favorable orientation relationships with the austenite than the σ phase, as a result, the σ phase is the last phase appearing during aging. Besides, there is a view that the formation of the intermetallic phase increases the solubility of carbon in the austenite matrix, which leads to the gradual dissolution of $M_{23}C_6$ carbide.

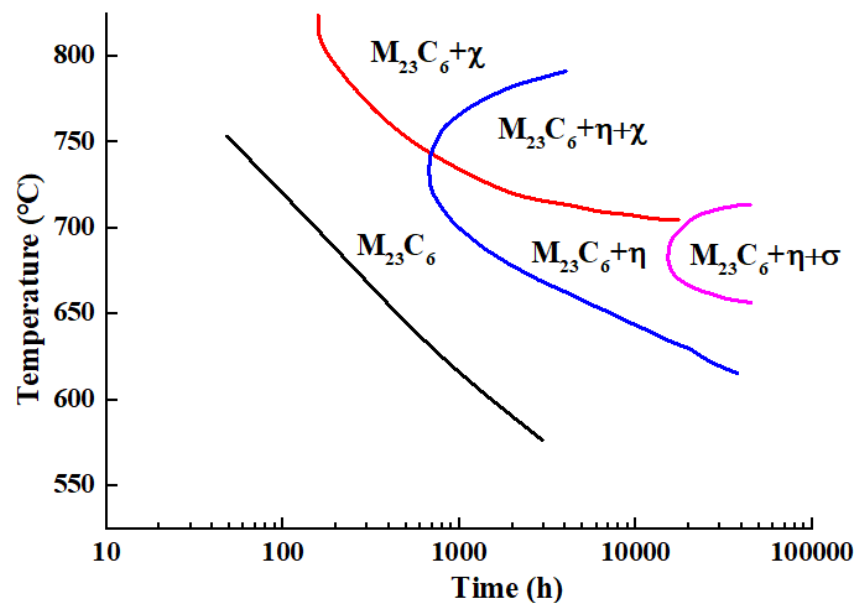


Figure 4. Time-temperature-precipitation diagram of solution-treated 316L austenitic stainless steel. Reproduced from Lai, J.K.L. [19].

The precipitation behaviors have been extensively investigated according to the available TTP diagrams of conventional austenitic stainless steel, and the mechanism at the early stage is fairly well understood. Nevertheless, the precipitation behaviors of new-developed advanced austenitic stainless steels are rather obscure. Composition optimization in these new-developed steels can significantly alter the precipitation kinetics. Impacts of several factors such as nitrogen alloying, the mono-/multi-stabilization elements effect, phosphorus addition and boron addition are present in the following.

5.2. Effect of Nitrogen Alloying

High carbon grades of 304 and 316 are used extensively for out-of-core structural components in the early sodium-cooled fast reactor. Afterward, carbon content is limited to a low value to prevent sensitization during welding so as to decrease the risks of intergranular corrosion and stress-corrosion cracking. Since low carbon grade steels have lower strength than normal grades, the nitrogen-alloyed versions designated as Type 304, Type 316, 304L(N), 316L(N), 316FR and 316KD are developed for the high-temperature components in the countries developing fast reactors.

Despite a reduction in the carbon content in the modified austenitic stainless steel resulting in a higher tendency to form δ -ferrite, nitrogen addition effectively prevents δ -ferrite formation due to nitrogen being a strong austenite stabilizer according to the aforementioned Ni_{eq} equation. Meanwhile, influences of nitrogen content on mechanical properties demonstrate that the optimum amount of nitrogen can substantially improve the tensile strength, creep rupture strength and fatigue life [17,21,53–57]. The beneficial effects of nitrogen have been widely studied, and the strengthening mechanisms are summarized: (i) Nitrogen has a strong solid-solution hardening effect. Nitrogen produces a higher dilation than carbon due to the difference in electron exchange characteristics between

carbon and nitrogen. The introduction of enhanced elastic distortions into the austenitic crystal lattice gives rise to stronger pinning effects on dislocation motion. The variations of Young's modulus with nitrogen content demonstrate a significant increase in modulus with increasing nitrogen content [57]. It is estimated that the strengthening effect of nitrogen is more than twice as effective as carbon [58]; (ii) nitrogen alters the carbide precipitation behavior. Unlike carbon, nitrogen does not present a noticeable grain boundary segregation tendency due to a weak affinity of nitrogen to grain boundaries. Nitrogen has been shown to delay the onset of $M_{23}C_6$ precipitation during thermal aging or creep, supported by an increase in the incubation time of $M_{23}C_6$ precipitation with increasing nitrogen content during aging in 316KD austenitic stainless steel (Figure 5). The reason is that chromium has a higher affinity for nitrogen than for carbon [59]. Moreover, nitrogen is known to reduce the coarsening rate of $M_{23}C_6$. Matsuo et al. [60] previously proposed that nitrogen can decrease the misfit between $M_{23}C_6$ and austenite, resulting in the retardation of carbide coalescence. This explanation is not consistent with the very small amount of nitrogen in $M_{23}C_6$ carbide. A more reasonable explanation is that the presence of nitrogen in a solid solution decreases the activity of chromium through the formation of chromium nitrides or Cr-N complexes and thus slows down the diffusivity of chromium [61]. However, there is no experimental evidence for this explanation yet. (iii) Nitrogen affects the high-temperature deformation mechanism. Dislocation evolution during deformation is directly correlated with the stacking fault energy (SFE). A new empirical expression to predict SFE from composition in austenitic stainless steels is proposed [62]:

$$\text{SFE (mJ}\cdot\text{m}^{-2}) = 2.2 + 1.9\text{Ni} - 2.9\text{Si} + 0.77\text{Mo} + 0.5\text{Mn} + 40\text{C} - 0.016\text{Cr} - 3.6\text{N} \quad (3)$$

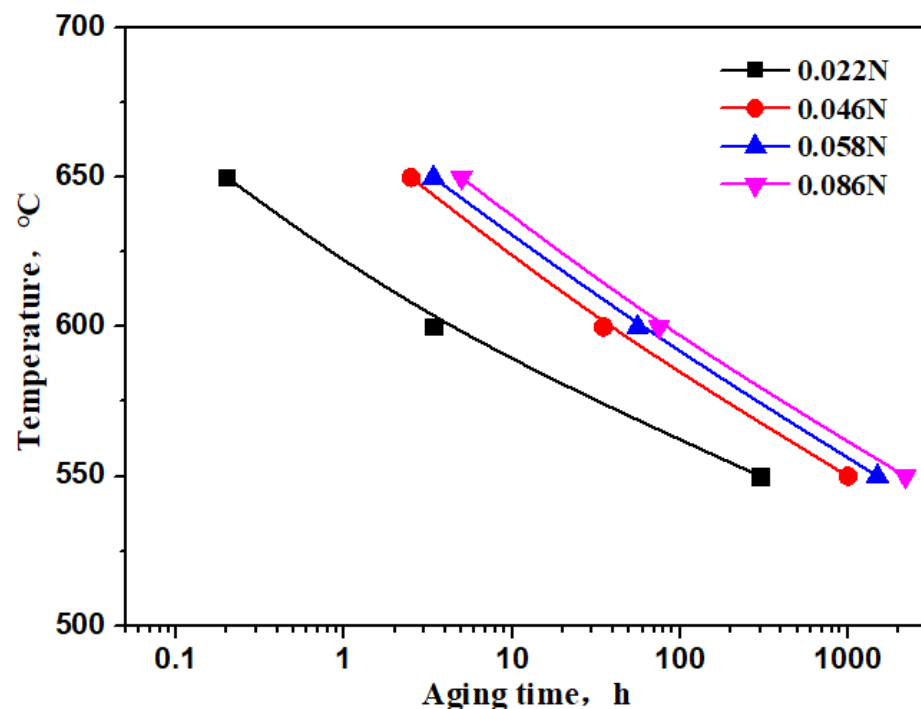


Figure 5. Effect of nitrogen content on the precipitation kinetics of $M_{23}C_6$ carbide in 316KD austenitic stainless steel.

It is shown that the addition of nitrogen decreases SFE value. Lower SFEs are known to be beneficial for creep properties because the more extended partial dislocations make cross-slip more difficult [63]. Microstructural observations after creep-fatigue tests of 316L and 316L(N) at 600 °C found that dislocation structures change from cell/subgrain to planar slip with the addition of nitrogen [55]. The suppression of cell/subgrain formation with increas-

ing nitrogen content is also observed after the creep test of 316L(N) at 650 °C [57]. Besides, the operation temperature of fast reactors is the most active temperature for the occurrence of dynamic strain aging (DSA), which is induced by the interaction between diffusing solute atoms and mobile dislocation during plastic deformation. Although DSA increases tensile strength through enhanced work-hardening ability, it is significantly detrimental to strain-controlled fatigue and creep-fatigue life [55,64–67]. The proposed mechanism is that DSA-induced inhomogeneous deformation reduces the crack initiation life, while DSA-induced hardening decreases the propagation life. As the strong interaction between nitrogen and chromium slows down the diffusion of chromium to mobile dislocations, the addition of nitrogen retards DSA [68,69]. As a consequence, fatigue and creep-fatigue life increase and the crack propagation rate decreases with the addition of nitrogen. Despite nitrogen having a high solubility in austenite in excess of 0.1 wt.% at a temperature above 550 °C [70], an upper limit of nitrogen content (~0.08 wt.%) is generally set to have no detrimental effect on weldability in Type 304, Type 316, 304L(N), 316L(N) and 316KD. A potential higher content is specified for 316FR in the JMSE code [12], but the actual nitrogen content in products is also limited to ~0.08 wt.% [71].

A comparison of creep rupture strength and strain-controlled low-cycle fatigue properties of low-carbon medium-nitrogen 316L(N) in RCC-MRx with medium-carbon medium-nitrogen Type 316 in ASME-NH at 650 °C is shown in Figure 6. The creep rupture strength data are available up to 300,000 h, and the fatigue life data up to 10^6 cycles are provided. The creep rupture strength of 316L(N) grade is lower than Type 316 at a high sustained stress level, while 316L(N) shows superior creep rupture strength than Type 316 at sustained stress levels lower than 310 MPa (Figure 6a). Meanwhile, the fatigue life of 316L(N) is higher than Type 316 as the total strain is lower than 0.7% (Figure 6b). In comparison, 316L(N) is preferred over Type 316 in the future design of sodium-cooled fast reactors to fulfill the requirement for extending the design life from the current level of 40 years to 60 years.

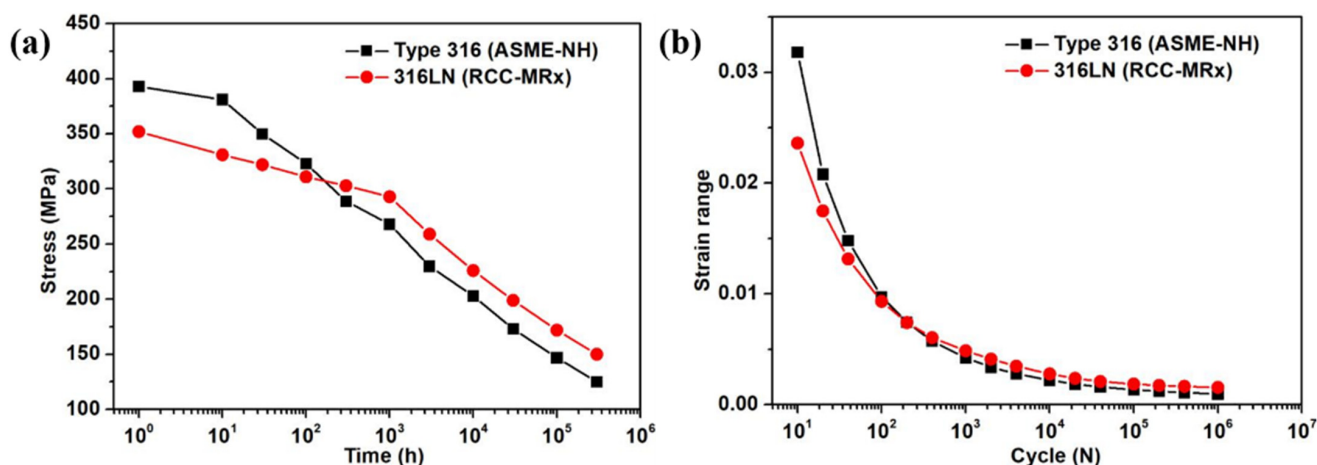


Figure 6. Comparison of (a) creep rupture strength and (b) fatigue life at 650 °C of 316L(N) in RCC-MRx and Type 316 in ASME-NH.

5.3. Effect of Mono-/Multi-Stabilization Elements

In order to inhibit the precipitation of $M_{23}C_6$ carbides, the addition of strong carbide-forming alloying elements can result in the formation of MC carbides primarily in austenitic stainless steels [72]. Niobium, titanium and vanadium are the well-known strong MC carbide-forming elements. The fine dispersion of MC carbides not only serves as an obstacle to dislocation movement to improve the high-temperature creep strength but also suppresses the radiation-induced void development during irradiation. Therefore, optimized niobium and titanium contents play a dominant role in swelling resistance and creep strength.

Titanium has the greatest influence on the swelling behaviors of austenitic stainless steels under neutron irradiation among the general stabilizing element (Ti, Nb, V) [73]. Ti-stabilized austenitic stainless steels such as 316Ti, D9, 15/15Ti, 1.4970 and ChS68 are developed for the in-core components of fast reactors. Titanium in the solid solution diffuses toward dislocation to form a Cottrell-type atmosphere, which can stabilize the pre-existing dislocation network under irradiation [74]. Furthermore, the formation of fine TiC carbides consumes a fraction of titanium from solid solution, and these fine TiC carbides can pin the dislocation and act as defect sinks and recombination sites [75]. In the presence of phosphorus, the formation of fine (Fe,Ti)₂P-type phosphide particles is also beneficial for the suppression of swelling, which will be reviewed in Section 5.4. It is worth noting that the final cold working with an optimum of 20% is required for Ti-stabilized austenitic stainless steels in order to promote the formation of fine TiC on dislocations [76]. Recently, the advantage of multi-stabilization (Nb, Ti, V) has also been proposed. Multi-stabilization strategies significantly increase the void swelling incubation dose, because the replacement of titanium in MC carbides and M₂P phosphide by niobium and vanadium can leave more and more Ti in a solid solution. The newly multi-stabilized (Nb, Ti, V) HT-UPS exhibits better-swelling resistance than Ti-stabilized D9 [77]. Modified ChS68 with three stabilizing elements of niobium, titanium and vanadium has been developed in Russia to reduce the swelling rate at enhanced damaging doses [78].

Upon exposure to high temperatures, the precipitation of secondary MC carbides in the austenite matrix is also responsible for the excellent mechanical properties [79]. The stabilization ratio $SR = (Ti + Nb + V)/C$ is extremely important so as to maximize the strengthening mechanism and avoid the formation of a detrimental phase. The influence of the Ti/C ratio on the creep properties of D9 at 700 °C shows that a peak in the rupture strength and a minimum in the steady creep rate is found in steel with $Ti/C \approx 6$ because of a higher volume fraction of fine secondary TiC carbides (Figure 7) [80]. A lower Ti/C ratio ($Ti/C \approx 4$) leads to the formation of M₂₃C₆ and M₆C, while a higher Ti/C ratio ($Ti/C \approx 9$) promotes the formation of primary TiC and intermetallic Fe₂Mo during creep. In the Nb-stabilized austenitic stainless steels such as Type 347 and TP347HFG, the superior creep strength at high temperatures is attributed to the precipitation of secondary NbC carbides [81]. Usually, a specified Nb/C ratio of 8~11 is controlled to optimize the secondary NbC precipitation. A higher Nb/C ratio results in the formation of coarse primary NbC carbides during the solidification process and the precipitation of the Fe₂Nb Laves phase after long-term aging/creep [82]. Small cracks and voids are detected along coarse NbC carbides, which deteriorates the fracture resistance. Coarse primary NbC is very difficult to be eliminated through subsequent hot working and heat treatment, even near the melting temperature. Furthermore, its formation consumes a large amount of Nb from the solid solution, which is unfavorable for the precipitation of secondary fine NbC [83]. A more restrictive specification on the content of carbon and niobium to obtain the optimum Nb/C ratio is also needed.

To obtain a higher density of MX carbide during subsequent precipitation, solution treatment is adopted to promote the dissolution of stabilizing elements in the solid solution as much as possible. Therefore, the solubility product of $[M][X]$ is an important factor in optimizing the content of the stabilizing element. The estimated solubility product curves show that the solubility product of TiC is much larger than that of NbC (Figure 8). In comparison, a higher amount of TiC can be dissolved into a solid solution after the solution is treated at the same temperature, resulting in the larger precipitation hardening in Ti-stabilized austenitic stainless steels during creep. Meanwhile, TiC shows a lower coarsening rate than NbC during creep because of the smaller lattice mismatch between TiC and austenite matrix [79]. However, TiO₂ and TiN inclusions are frequently formed during the casting of Ti-stabilized austenitic stainless steels since Ti has a high affinity for O and N from the air, molten steel, or molten slag [84]. Besides the addition of mono-stabilized elements and further improvements in the creep resistance have been made by the multi-stabilization of niobium, titanium and vanadium through the formation of

M(C,N) carbonitrides and the Z phase (CrNbN) in advanced HT-UPS and NF709, which are considered as attractive candidate construction materials for major components (reactor vessel, core supports, intermediate heat exchanger, etc.) of advanced burner reactors and sodium-cooled fast reactors [85].

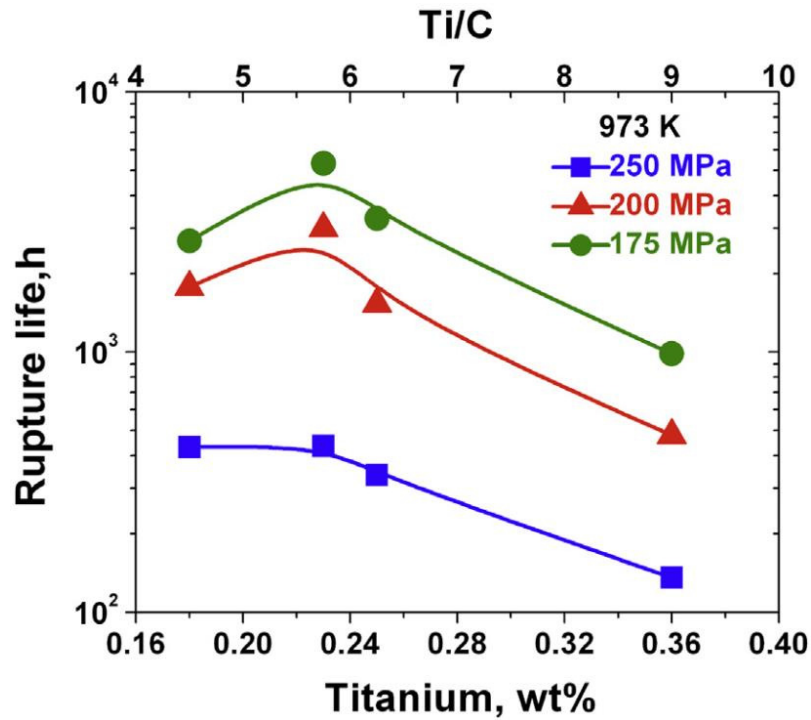


Figure 7. Effect of Ti/C ratio on the creep rupture life of Ti-modified D9 in the range of 175–250 MPa at 700 °C [80].

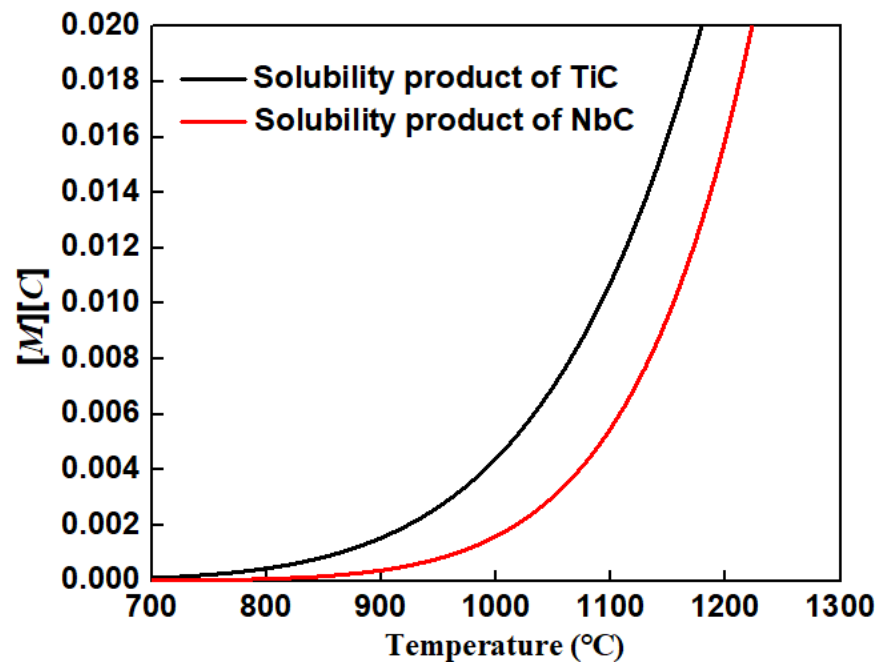


Figure 8. The estimated solubility product curves of TiC and NbC in austenite.

5.4. Effect of Phosphorus Addition

Phosphorus has long been considered an impurity element in austenitic stainless steel, thus the upper limit on phosphorus content (<0.05 wt.%) is generally specified. However,

concerns have been raised about the beneficial effect of phosphorus on the mechanical properties and irradiation properties of austenitic stainless steel since the 1980s.

Firstly, variation in phosphorus content can affect the precipitation behavior of carbides and intermetallic phases. It is found that the amount of Laves phases within grains and $M_{23}C_6$ carbide on grain boundaries are both reduced with an increase in phosphorus content [71,86]. For the cold-worked 316Ti, the beneficial effects of phosphorus on the improvement of mechanical properties are due to phosphorus being conducive to the precipitation of finely distributed $M_{23}C_6$ carbides within grains during annealing treatment between 600 °C and 800 °C [87,88]. In addition, phosphorus has been found to delay the formation of the intermetallic phase because of the abundant nucleation of $M_{23}C_6$ carbide. The creep rupture properties of Type 316 containing 0.002~0.052% phosphorus at 550 °C and 600 °C reveal that an increase in phosphorus content enhances rupture strength, and the effect is more pronounced after long-term creep tests [86].

Secondly, phosphorus is shown to be much more effective in suppressing swelling and improving the irradiation creep resistance of austenitic stainless steels. Investigations on irradiation creep in AISI 316 pressurized tubes show that phosphorus is much more effective in reducing swelling on a per-atom basis than other common solutes (Figure 9) [89–91] because phosphorus can increase the diffusivity of matrix solvent and the equilibrium vacancy concentration by orders of magnitude. Temperature dependence of void swelling in alloy D9 with a phosphorus content of 0.026% and 0.048% in the range of 427–697 °C exhibits that void swelling is found to be lower with a higher phosphorus content, and swelling at the peak temperature is also less [17]. Moreover, swelling can be suppressed through the formation of a very fine dispersion of stable M_2P phosphide particles during thermal aging/irradiation in phosphorous-modified Fe-Ni-Cr alloys, which is attributed to the phosphide-matrix interface providing nucleation sites for a high density of helium bubbles [92,93].

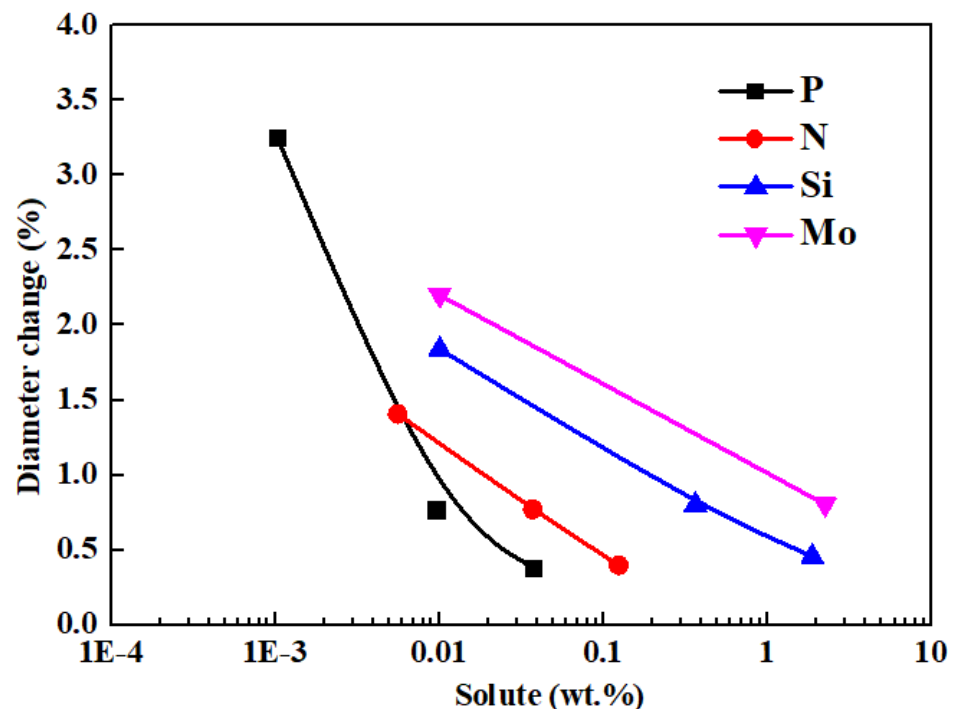


Figure 9. Effect of solutes on irradiation creep of pressurized tubes of 10% cold-worked AISI 316 in ERB-II at 450 °C, 23 dpa and a hoop stress of 172 MPa. Reproduced from Garner, F.A. [90].

Based on the effect of phosphorus addition on mechanical properties and irradiation properties, modified austenitic stainless steel with a controlled phosphorus content has been developed for fast reactors. In France, Germany and India, modified versions of D9,

15/15Ti and 1.4970 having rather high contents of phosphorus (0.04 wt.%) are developed for in-core components [17]. Modified austenitic stainless steels with a controlled amount of phosphorus (0.015~0.03 wt.%) are developed on the basis of ChS68, which is used as a standard material for fuel element cladding for the BN-600 sodium-cooled fast reactor in Russia [78]. The lower and upper limits of phosphorus content (0.02~0.045 wt.%) are specified in 316FR, which is developed for reactor vessels and the internals of sodium-cooled fast reactors in Japan [71].

5.5. Effect of Boron Addition

Boron was previously considered a trace solute impurity in austenitic stainless steels. Boron has a strong tendency to segregate at grain boundaries owing to the large free energies of segregation. Unlike many other segregants, it does not cause grain boundary embrittlement. Afterward, boron was regarded as a kind of micro-alloyant to improve the mechanical properties of austenitic stainless steels.

Boron segregations at grain boundaries are detected after solution treatment in austenitic stainless steel, and the segregation behaviors are dominated by the non-equilibrium segregation mechanism [94,95]. Numerous investigations demonstrate that the addition of boron significantly increases the high-temperature creep strength in 304, 316, 347 and DIN 1.4970 [96–101]. The beneficial effect of boron on creep resistance can be divided into three respects. Firstly, the addition of boron is beneficial for carbide precipitation. Boron being an interstitial element reduces the solubility of carbon in austenite, consequently, carbide precipitation on dislocations is promoted during creep, which is responsible for the enhanced creep deformation resistance. Significant effects of boron on promoting the precipitation of finely dispersed carbides are observed in cold-worked austenitic stainless steel [97]. Secondly, the addition of boron alters the character of the matrix/precipitates interface. The incorporation of boron into $M_{23}C_6$ carbide to form $M_{23}(C,B)_6$ increases the stability of carbides, so as to increase grain boundary sliding resistance [98]. The resultant decrease in the mismatch between carbide and austenite matrix lowers the matrix/precipitates interface energy, thereby suppressing creep cavity nucleation. Lastly, the addition of boron suppresses creep cavity growth. Boron is found to segregate on the creep cavity surface by Auger electron spectroscopy analyses. The segregation of boron is expected to significantly reduce self-diffusivity along the cavity surface [99–101], which is considered to impart a high reduction in cavity growth rate. Firm segregation of boron along the cavity surface provides the steel with the function of a self-healing effect for creep cavitations.

Boron has relatively low solubility in the austenite lattice due to its atomic size. The calculated solubility of boron in Fe-16Cr-13Ni austenitic stainless steel confirms that the maximum solubility is ~200 ppm at eutectic temperatures and significantly decreases to ~20 ppm at 900 °C [52]. During welding operations, the formation of a eutectic phase with a low-melting point causes hot cracking when a higher content of boron is added. Furthermore, M_2B precipitation easily takes place during creep if the boron content exceeds ~30 ppm in the austenitic stainless steels [102]. The effect of M_2B precipitation on mechanical properties is still not very clear. Nevertheless, the formation of M_2B is prone to remove boron from a solid solution, causing a deterioration in the self-healing function for creep cavitation. Optimized boron content is specified in most modified austenitic stainless steels for fast reactors, including Type 316, 316L(N) and NF709 for out-of-core components, and 1.4970, ChS68 and HT-UPS for in-core components.

6. Conclusions

Based on the experience feedback from the fast reactor constructions and operation worldwide, modified austenitic stainless steels for in-core and out-of-core components are developed from the first candidate 300-series steels. The design of appropriate microstructure is crucial to improve the material performance, and key metallurgical features including δ -ferrite content, grain size and secondary phase precipitation pertinent to

austenitic stainless steel are comprehensively reviewed in this paper. δ -ferrite content and grain size are the two key final metallurgical features of products, which are closely correlated with the fabrication program. Their influences on mechanical properties, especially creep and fatigue properties pertinent to fast reactors are assessed. δ -ferrite content must be controlled or even limited to have a stable microstructure. An intermediate value or maximum value is specified for grain size, and isolated grains with extremely large sizes must be avoided. Secondary phase precipitation is mainly responsible for the changes in mechanical properties and irradiation resistance during long-term exposure to high temperatures, which strongly depends on some major elements including nitrogen, stabilization elements, phosphorus and boron. The impacts of these factors on secondary-phase precipitation behaviors are reviewed in detail. The optimum nitrogen content, stabilization ratio, phosphorus content and boron content are beneficial for creep rupture strength, fatigue life and irradiation resistance. A modified version is developed through a precise specification of nitrogen content, phosphorus content, boron content, stabilization ratio, δ -ferrite content and grain size.

The technical database of the modified austenitic stainless steels is much less than conventional 304SS and 316SS until now. The secondary phase precipitation mechanisms at the early stage are fairly well understood, but precipitation kinetics for longer times are rather obscure. Especially, long-term data are dramatically needed to demonstrate the material behaviors to fulfill the planned lifetime extension requirements in fuel and reactor.

Author Contributions: Conceptualization, S.C. (Shenghu Chen) and L.R.; methodology, S.C. (Shenghu Chen); formal analysis, S.C. (Shenghu Chen); investigation, S.C. (Shenghu Chen), A.X. and X.L.; resources, S.C. (Shenghu Chen), A.X., X.L. and S.C. (Sihan Chen); data curation, S.C. (Shenghu Chen), A.X., X.L. and S.C. (Sihan Chen); writing—original draft preparation, S.C. (Shenghu Chen), A.X., X.L. and S.C. (Sihan Chen); writing—review and editing, S.C. (Shenghu Chen), C.Y., H.J. and L.R.; visualization, S.C. (Shenghu Chen); supervision, S.C. (Shenghu Chen) and L.R.; project administration, S.C. (Shenghu Chen) and L.R.; funding acquisition, S.C. (Shenghu Chen) and L.R. All authors have read and agreed to the published version of the manuscript.

Funding: This research was funded by National Natural Science Foundation of China (No. 51871218), CNNC Science Fund for Talented Young Scholars, and LingChuang Research Project of China National Nuclear Corporation.

Data Availability Statement: Not applicable.

Conflicts of Interest: The authors declare no conflict of interest.

References

1. Buckthorpe, D. Introduction to Generation IV nuclear reactors. In *Structural Materials for Generation IV Nuclear Reactors*; Yvon, P., Ed.; Elsevier Ltd.: Amsterdam, The Netherlands, 2017; pp. 1–22.
2. Kelly, J.E. Generation IV International Forum: A decade of progress through international cooperation. *Prog. Nucl. Energ.* **2014**, *77*, 240–246. [[CrossRef](#)]
3. Locatelli, G.; Mancini, M.; Todeschini, N. Generation IV nuclear reactors: Current status and future prospects. *Energ. Policy* **2013**, *61*, 1503–1520. [[CrossRef](#)]
4. Abram, T.; Ion, S. Generation-IV nuclear power: A review of the state of the science. *Energ. Policy* **2008**, *36*, 4323–4330. [[CrossRef](#)]
5. Aoto, K.; Dufour, P.; Yang, H.; Glatz, J.P.; Kim, Y.; Ashurko, Y.; Hill, R.; Uto, N. A summary of sodium-cooled fast reactor development. *Prog. Nucl. Energ.* **2014**, *77*, 247–265. [[CrossRef](#)]
6. Pioro, I.L. Introduction: Generation IV international forum. In *Handbook of Generation IV Nuclear Reactors*; Pioro, I.L., Ed.; Woodhead Publishing: Duxford, UK, 2016; pp. 37–54.
7. Guérin, Y.; Was, G.S.; Zinkle, S.J. Materials challenges for advanced nuclear energy systems. *MRS Bull.* **2009**, *34*, 10–19.
8. Yvon, P.; Carré, F. Structural materials challenges for advanced reactor systems. *J. Nucl. Mater.* **2009**, *385*, 217–222. [[CrossRef](#)]
9. Murty, K.L.; Charit, I. Structural materials for Gen-IV nuclear reactors: Challenges and opportunities. *J. Nucl. Mater.* **2008**, *383*, 189–195. [[CrossRef](#)]
10. Natesan, K.; Li, M.; Majumdar, S.; Nanstad, R.K.; Sham, T.-L. Materials and code qualification needs for sodium-cooled fast reactors. In Proceedings of the International Conference on Fast Reactors and Related Fuel Cycles (FR09), Kyoto, Japan, 7 December 2009.

11. ASME Boiler and Pressure Vessel Code. Section III, Rules for Construction of Nuclear Power Plant Components, Division 1, Subsection NH, Class 1 Components in Elevated Temperature Service; The American Society of Mechanical Engineers: New York, NY, USA, 2015.
12. JSME, Code for Nuclear Power Generation Facilities, Rules on Design and Construction for Nuclear Power Plants, Section II Fast Reactor Standards (in Japanese); The Japan Society of Mechanical Engineers: Tokyo, Japan, 2016.
13. RCC-MRx. Design and Construction Rules for Mechanical Components of Nuclear Installations: High Temperature, Research and Fusion Reactors; AFCEN: Paris, France, 2015.
14. Was, G.S.; Ukai, S. Austenitic stainless steels. In *Structural Alloys for Nuclear Energy Applications*; Odette, G.R., Zinkle, S.J., Eds.; Elsevier: Boston, MA, USA, 2019; pp. 293–347.
15. Karthik, V.; Murugan, S.; Parameswaran, P.; Venkiteswaran, C.N.; Gopal, K.A.; Muralidharan, N.G.; Saroja, S.; Kasiviswanathan, K.V. Austenitic stainless steels for fast reactors—Irradiation experiments, property evaluation and microstructural studies. *Energy Procedia* **2011**, *7*, 257–263. [[CrossRef](#)]
16. Gong, X.; Short, M.P.; Auger, T.; Charalampopoulou, E.; Lambrinou, K. Environmental degradation of structural materials in liquid lead-and lead-bismuth eutectic-cooled reactors. *Prog. Mater. Sci.* **2022**, *126*, 100920. [[CrossRef](#)]
17. Jayakumar, T.; Mathew, M.; Laha, K.; Sandhya, R. Materials development for fast reactor applications. *Nucl. Eng. Des.* **2013**, *265*, 1175–1180. [[CrossRef](#)]
18. Horak, J.; Sikka, V.; Raske, D. Review of mechanical properties and microstructures of Types 304 and 316 stainless steel after long-term aging. In Proceedings of the IAEA Specialists on Mechanical Properties of Structural Materials, Chester, UK, 10 October 1983.
19. Lai, J.K.L. A study of precipitation in AISI type 316 stainless steel. *Mater. Sci. Eng.* **1983**, *58*, 195–209. [[CrossRef](#)]
20. Lai, J.K.L.; Chastell, D.J.; Flewitt, P.E.J. Precipitate phases in type 316 austenitic stainless steel resulting from long-term high temperature service. *Mater. Sci. Eng.* **1981**, *49*, 19–29. [[CrossRef](#)]
21. Mathew, M.D. Evolution of creep resistant 316 stainless steel for sodium cooled fast reactor applications. *Trans. Indian Inst. Met.* **2010**, *63*, 151–158. [[CrossRef](#)]
22. RMC. Design and Construction Rules for Mechanical Components for the FBR Nuclear Islands, RCC-MR, Section 3-Examination Methods; AFCEN: Paris, France, 2007; p. 1341.
23. Guiraldenq, P.; Olivier, H.D. The genesis of the Schaeffler diagram in the history of stainless steel. *Metall. Res. Technol.* **2017**, *114*, 613. [[CrossRef](#)]
24. Zhang, M.; Lu, Y.; Chen, S.; Rong, L.; Lu, H. Effect of dilution ratio of the first 309l cladding layer on the microstructure and mechanical properties of weld joint of connecting pipe-Nozzle to safe-End in nuclear power plant. *Acta Metall. Sin.* **2020**, *56*, 1057–1066.
25. Ferrandini, P.L.; Rios, C.T.; Dutra, A.T.; Jaime, M.A.; Mei, P.R.; Caram, R. Solute segregation and microstructure of directionally solidified austenitic stainless steel. *Mater. Sci. Eng. A* **2006**, *435*, 139–144. [[CrossRef](#)]
26. Padilha, A.F.; Tavares, C.F.; Martorano, M.A. Delta ferrite formation in austenitic stainless steel castings. *Mater. Sci. Forum* **2013**, *730*, 733–738. [[CrossRef](#)]
27. Koseki, T.; Flemings, M.C. Solidification of undercooled Fe-Cr-Ni alloys: Part III. Phase selection in chill casting. *Metall. Mater. Trans. A* **1997**, *28*, 2385–2395. [[CrossRef](#)]
28. Wang, Q.; Chen, S.; Rong, L. δ -ferrite formation and its effect on the mechanical properties of heavy-section AISI 316 stainless steel casting. *Metall. Mater. Trans. A* **2020**, *51*, 2998–3008. [[CrossRef](#)]
29. Byun, T.S.; Collins, D.A.; Lach, T.G.; Carter, E.L. Degradation of impact toughness in cast stainless steels during long-term thermal aging. *J. Nucl. Mater.* **2020**, *542*, 152524. [[CrossRef](#)]
30. Badyka, R.; Monnet, G.; SAILLET, S.; Domain, C.; Pareige, C. Quantification of hardening contribution of G-Phase precipitation and spinodal decomposition in aged duplex stainless steel: APT analysis and micro-hardness measurements. *J. Nucl. Mater.* **2019**, *514*, 266–275. [[CrossRef](#)]
31. Byun, T.S.; Yang, Y.; Overman, N.R.; Busby, J.T. Thermal aging phenomena in cast duplex stainless steels. *JOM* **2016**, *68*, 507–516. [[CrossRef](#)]
32. Tseng, C.C.; Shen, Y.; Thompson, S.W.; Mataya, M.C.; Krauss, G. Fracture and the formation of sigma phase, M23C6, and austenite from delta-ferrite in an AISI 304L stainless steel. *Metall. Mater. Trans. A* **1994**, *25*, 1147–1158. [[CrossRef](#)]
33. Warren, A.D.; Griffiths, I.J.; Harniman, R.L.; Flewitt, P.E.J.; Scott, T.B. The role of ferrite in Type 316H austenitic stainless steels on the susceptibility to creep cavitation. *Mater. Sci. Eng. A* **2015**, *635*, 59–69. [[CrossRef](#)]
34. Wei, S.; Zhao, L.; Gao, D.; Lu, S. Microstructure evolution and mechanical properties of 316H weld metal during aging. *Mater. Sci. Technol.* **2020**, *36*, 793–804. [[CrossRef](#)]
35. Wang, Q.; Chen, S.; Lv, X.; Jiang, H.; Rong, L. Role of δ -ferrite in fatigue crack growth of AISI 316 austenitic stainless steel. *J. Mater. Sci. Technol.* **2022**, *114*, 7–15. [[CrossRef](#)]
36. Sourmail, T. Precipitation in creep resistant austenitic stainless steels. *Mater. Sci. Technol.* **2001**, *17*, 1–14. [[CrossRef](#)]
37. Chen, S.; Wang, Q.; Jiang, H.; Rong, L. Effect of δ -ferrite on Hot Deformation and Recrystallization of 316KD Austenitic Stainless Steel for Sodium-Cooled Fast Reactor Application. *Acta Metall. Sin.* **2023**. [[CrossRef](#)]
38. Armstrong, R.W. The influence of polycrystal grain size on several mechanical properties of materials. *Metall. Mater. Trans. B* **1970**, *1*, 1169–1176. [[CrossRef](#)]

39. Singh, K.K.; Sangal, S.; Murty, G.S. Hall–Petch behaviour of 316L austenitic stainless steel at room temperature. *Mater. Sci. Technol.* **2002**, *18*, 165–172. [[CrossRef](#)]
40. Chen, S.; Zhao, M.; Rong, L. Effect of grain size on the hydrogen embrittlement sensitivity of a precipitation strengthened Fe–Ni based alloy. *Mater. Sci. Eng. A* **2014**, *594*, 98–102. [[CrossRef](#)]
41. Mannan, S.L.; Rodriguez, P. Effect of grain size on creep rate in type 316 stainless steel at 873 and 973 K. *Metal Sci.* **1983**, *17*, 63–69. [[CrossRef](#)]
42. Nakazawa, T.; Komatsu, H.; Takahashi, Y.; Date, S. Microstructure and grain size dependence of creep and creep-fatigue properties of low carbon medium nitrogen type 316 steel. *Tetsu-to-Hagané* **1998**, *84*, 142–147. [[CrossRef](#)] [[PubMed](#)]
43. Lee, Y.S.; Kim, D.W.; Lee, D.Y.; Ryu, W.S. Effect of grain size on creep properties of type 316LN stainless steel. *Met. Mater. Int.* **2001**, *7*, 107–114. [[CrossRef](#)]
44. Yamaguchi, K.; Kanazawa, K. Influence of grain size on the low-cycle fatigue lives of austenitic stainless steels at high temperatures. *Metall. Mater. Trans. A* **1980**, *11*, 1691–1699. [[CrossRef](#)]
45. McMurtrey, M.; Carroll, L.; Wright, J. *Microstructural Effects on Creep-Fatigue Life of Alloy 709*; Idaho National Lab. (INL): Idaho Falls, ID, USA, 2017; No. INL/EXT-17-41079.
46. Barr, C.M.; El-Atwani, O.; Kaoumi, D.; Hattar, K. Interplay Between Grain Boundaries and Radiation Damage. *JOM* **2019**, *71*, 1233–1244. [[CrossRef](#)]
47. Shirdel, M.; Mirzadeh, H.; Parsa, M.H. Abnormal grain growth in AISI 304L stainless steel. *Mater. Charact.* **2014**, *97*, 11–17. [[CrossRef](#)]
48. Chen, S.; Rong, L. Microstructure Evolution During Solution Treatment and Its Effects on the Properties of Ni-Fe-Cr Alloy. *Acta Metall. Sin.* **2017**, *54*, 385–392.
49. Shirdel, M.; Mirzadeh, H.; Habibi, P.M. Microstructural Evolution during Normal/Abnormal Grain Growth in Austenitic Stainless Steel. *Metall. Mater. Trans. A* **2014**, *45*, 5185–5193. [[CrossRef](#)]
50. Najafkhani, F.; Kheiri, S.; Pourbahari, B.; Mirzadeh, H. Recent advances in the kinetics of normal/abnormal grain growth: A review. *Archiv. Civ. Mech. Eng.* **2021**, *21*, 1–20. [[CrossRef](#)]
51. Plaut, R.L.; Herrera, C.; Escriba, D.M.; Rios, P.R.; Padilha, A.F. A short review on wrought austenitic stainless steels at high temperatures: Processing, microstructure, properties and performance. *Mater. Res.* **2007**, *10*, 453–460. [[CrossRef](#)]
52. Padilha, A.F.; Rios, P.R. Decomposition of austenite in austenitic stainless steels. *ISIJ Inter.* **2002**, *42*, 325–327. [[CrossRef](#)]
53. Ganesan, V.; Mathew, M.D.; Sankara, R.K.B. Influence of nitrogen on tensile properties of 316LN SS. *Mater. Sci. Technol.* **2009**, *25*, 614–618. [[CrossRef](#)]
54. Mathew, M.D.; Sasikala, G.; Rao, K.B.S.; Mannan, S.L. Influence of carbon and nitrogen on the creep properties of type 316 stainless steel at 873 K. *Mater. Sci. Eng. A* **1991**, *148*, 253–260. [[CrossRef](#)]
55. Kim, D.W.; Chang, J.H.; Ryu, W.S. Evaluation of the creep–fatigue damage mechanism of Type 316L and Type 316LN stainless steel. *Inter. J. Pres. Ves. Pip.* **2008**, *85*, 378–384. [[CrossRef](#)]
56. Kumar, J.G.; Chowdary, M.; Ganesan, V.; Paretkar, R.K.; Rao, K.B.S.; Mathew, M.D. High temperature design curves for high nitrogen grades of 316LN stainless steel. *Nucl. Eng. Des.* **2010**, *240*, 1363–1370. [[CrossRef](#)]
57. Mathew, M.D.; Laha, K.; Ganesan, V. Improving creep strength of 316L stainless steel by alloying with nitrogen. *Mater. Sci. Eng. A* **2012**, *535*, 76–83. [[CrossRef](#)]
58. Byrnes, M.L.G.; Grujicic, M.; Owen, W.S. Nitrogen strengthening of a stable austenitic stainless steel. *Acta Metall.* **1987**, *35*, 1853–1862. [[CrossRef](#)]
59. Shankar, P.; Sundararaman, D.; Ranganathan, S. Clustering and ordering of nitrogen in nuclear grade 316LN austenitic stainless steel. *J. Nucl. Mater.* **1998**, *254*, 1–8. [[CrossRef](#)]
60. Matsuo, T.; Shinoda, T.; Tanaka, R. Effect of nitrogen, boron and phosphorous on high temperature strength of 18Cr-10Ni and 18Cr-10Ni-Mo austenitic steels bearing small amounts of titanium and niobium. *Tetsu-to-Hagane* **1973**, *59*, 907–918. [[CrossRef](#)]
61. Kamachi, M.U.; Shankar, P.; Sundararaman, D.; Dayal, R.K. Microstructural and electrochemical studies in thermally aged type 316LN stainless steels. *Mater. Sci. Technol.* **1999**, *15*, 1451–1453. [[CrossRef](#)]
62. De Bellefon, G.M.; Van Duysen, J.C.; Sridharan, K. Composition-dependence of stacking fault energy in austenitic stainless steels through linear regression with random intercepts. *J. Nucl. Mater.* **2017**, *492*, 227–230. [[CrossRef](#)]
63. Dieter, G.E. *Mechanical Metallurgy*; McGraw-Hill: New York, NY, USA, 1976.
64. Lv, X.; Chen, S.; Wang, Q.; Jiang, H.; Rong, L. Temperature Dependence of Fracture Behavior and Mechanical Properties of AISI 316 Austenitic Stainless Steel. *Metals* **2022**, *12*, 1421. [[CrossRef](#)]
65. Hong, S.G.; Lee, K.O.; Lee, S.B. Dynamic strain aging effect on the fatigue resistance of type 316L stainless steel. *Int. J. Fatigue* **2005**, *27*, 1420–1424. [[CrossRef](#)]
66. Hong, S.G.; Lee, S.B. Dynamic strain aging under tensile and LCF loading conditions, and their comparison in cold worked 316L stainless steel. *J. Nucl. Mater.* **2004**, *328*, 232–242. [[CrossRef](#)]
67. Kim, D.W.; Kim, W.G.; Ryu, W.S. Role of dynamic strain aging on low cycle fatigue and crack propagation of type 316L (N) stainless steel. *Int. J. Fatigue* **2003**, *25*, 1203–1207. [[CrossRef](#)]
68. Choudhary, B.K. Activation energy for serrated flow in type 316L (N) austenitic stainless steel. *Mater. Sci. Eng. A* **2014**, *603*, 160–168. [[CrossRef](#)]

69. Kim, D.W.; Ryu, W.S.; Hong, J.H.; Choi, S. Effect of nitrogen on the dynamic strain ageing behaviour of type 316L stainless steel. *J. Mater. Sci.* **1998**, *33*, 675–679. [[CrossRef](#)]
70. Lai, J.K.L. A review of precipitation behaviour in AISI type 316 stainless steel. *Mater. Sci. Eng.* **1983**, *61*, 101–109. [[CrossRef](#)]
71. Onizawa, T.; Hashidate, R. Development of creep property equations of 316FR stainless steel and Mod. 9Cr-1Mo steel for sodium-cooled fast reactor to achieve 60-year design life. *Mech. Eng. J.* **2019**, *6*, 18-00477. [[CrossRef](#)]
72. Li, Y.; Liu, Y.; Liu, C.; Li, C.; Huang, Y.; Li, H.; Li, W. Carbide dissolution and precipitation in cold-rolled type 347H austenitic heat-resistant steel. *Mater. Lett.* **2017**, *189*, 70–73. [[CrossRef](#)]
73. Séran, J.; Le Flem, M. Irradiation-Resistant Austenitic Steels as Core Materials for Generation IV Nuclear Reactors. In *Structural Materials for Generation IV Nuclear Reactors*; Yvon, P., Ed.; Woodhead Publishing: Sawston, UK, 2017; p. 310.
74. Okita, T.; Wolfer, W.G.; Garner, F.A.; Sekimura, N. Effects of titanium additions to austenitic ternary alloys on microstructural evolution and void swelling. *Philos. Mag.* **2005**, *85*, 2033–2048. [[CrossRef](#)]
75. Cautaerts, N.; Delville, R.; Stergar, E.; Pakarinen, J.; Verwerft, M.; Yang, Y.; Hofer, C.; Schnitzer, R.; Lamm, S.; Felfer, P.; et al. The role of Ti and TiC nanoprecipitates in radiation resistant austenitic steel: A nanoscale study. *Acta Mater.* **2020**, *197*, 184–197. [[CrossRef](#)]
76. Ukai, S.; Uwaba, T. Swelling rate versus swelling correlation in 20% cold-worked 316 stainless steels. *J. Nucl. Mater.* **2003**, *317*, 93–101. [[CrossRef](#)]
77. Chi, X.; Xuan, Z.; Chen, Y.; Li, M.; Park, J.; Kenesei, P.; Almer, J.; Yang, Y. In-situ High-Energy X-ray Characterization of Neutron Irradiated HT-UPS Stainless Steel under Tensile Deformation. *Acta Mater.* **2018**, *156*, 330–341.
78. Vatulin, A.V.; Tselishchev, A.V. Structural steels for cores of fast neutron reactors. *Met. Sci. Heat Treat.* **2004**, *46*, 463–468. [[CrossRef](#)]
79. Abe, F.; Murata, M.; Miyazaki, H. Effect of TiC and NbC carbides on creep life of stainless steels. *Mater. High Temp.* **2019**, *36*, 37–45. [[CrossRef](#)]
80. Latha, S.; Mathew, M.D.; Parameswaran, P.; Nandagopal, M.; Mannan, S.L. Effect of titanium on the creep deformation behaviour of 14Cr–15Ni–Ti stainless steel. *J. Nucl. Mater.* **2011**, *409*, 214–220. [[CrossRef](#)]
81. Solenthaler, C.; Ramesh, M.; Uggowitzer, P.J.; Spolenak, R. Precipitation strengthening of Nb-stabilized TP347 austenitic steel by a dispersion of secondary Nb(C,N) formed upon a short-term hardening heat treatment. *Mater. Sci. Eng. A* **2015**, *647*, 294–302. [[CrossRef](#)]
82. Minami, Y.; Kimura, H.; Ihara, Y. Microstructural changes in austenitic stainless steels during long-term aging. *Mater. Sci. Technol.* **1986**, *2*, 795–806. [[CrossRef](#)]
83. Xie, A.; Chen, S.; Wu, Y.; Jiang, H.; Rong, L. Homogenization temperature dependent microstructural evolution and mechanical properties in a Nb-stabilized cast austenitic stainless steel. *Mater. Char.* **2022**, *194*, 112384. [[CrossRef](#)]
84. Zhou, L.; Pan, Z.; Wang, W.; Chen, J.; Xue, L.; Zhang, T.; Zhang, L. Interfacial Interactions between Inclusions Comprising TiO₂ or TiN and the Mold Flux during the Casting of Titanium-Stabilized Stainless Steel. *Metall. Mater. Trans. B* **2020**, *51*, 85–94. [[CrossRef](#)]
85. Dalle, F.; Blat-Yrieix, M.; Dubiez-Le Goff, S.; Cabet, C.; Dubuisson, P. Conventional austenitic steels as out-of-core materials for Generation IV nuclear reactors. In *Structural Materials for Generation IV Nuclear Reactors*; Yvon, P., Ed.; Woodhead Publishing: Sawston, UK, 2017; p. 629.
86. Nakazawa, T.; Kimura, H.; Tendo, M.; Komatsu, H. Effects of Carbon, Molybdenum, and Phosphorus Contents on Creep Rupture Properties of Low Carbon Medium Nitrogen Type 316 Stainless Steels. *J. Jpn. Inst. Met.* **2000**, *64*, 926–933. [[CrossRef](#)] [[PubMed](#)]
87. Mandiang, Y.; Cizeron, G. Phosphorus effects on mechanical properties changes in type 316 Ti stainless steels. *Mater. Sci. Eng. A* **1996**, *206*, 241–248. [[CrossRef](#)]
88. Mandiang, Y.; Azilinson, D.; Adj, M.; Cizeron, G. Effect of phosphorus on stability of cold worked structure in 316Ti austenitic stainless steel. *Met. Sci. J.* **2000**, *16*, 399–407. [[CrossRef](#)]
89. Garner, F.A.; Mitchell, M.A. The complex role of phosphorus in the neutron-induced swelling of titanium-modified austenitic stainless steels. *J. Nucl. Mater.* **1992**, *187*, 223–229. [[CrossRef](#)]
90. Garner, F.A.; Brager, H.R. The role of phosphorus in the swelling and creep of irradiated austenitic alloys. *J. Nucl. Mater.* **1985**, *133*, 511–514. [[CrossRef](#)]
91. Watanabe, H.; Garner, F.A.; Muroga, T.; Yoshida, N. The influence of silicon and phosphorus additions on neutron induced microstructural evolution of Fe Cr Ni ternary alloys at 646–703 K. *J. Nucl. Mater.* **1995**, *225*, 76–84. [[CrossRef](#)]
92. Lee, E.H.; Mansur, L.K. A mechanism of swelling suppression in phosphorus-modified Fe-Ni-Cr alloys. *J. Nucl. Mater.* **1986**, *141–143*, 695–702. [[CrossRef](#)]
93. Lee, E.H.; Mansur, L.K. Fe–15Ni–13Cr austenitic stainless steels for fission and fusion reactor applications. II. Effects of minor elements on precipitate phase stability during thermal aging. *J. Nucl. Mater.* **2000**, *278*, 11–19. [[CrossRef](#)]
94. Karlsson, L.; Nordén, H.; Odellius, H. Non-equilibrium grain boundary segregation of boron in austenitic stainless steel-I. Large scale segregation behaviour. *Acta Metall.* **1988**, *36*, 1–12. [[CrossRef](#)]
95. Williams, T.M.; Stoneham, A.M.; Harries, D.R. The segregation of boron to grain boundaries in solution-treated Type 316 austenitic stainless steel. *Met. Sci. J.* **1976**, *10*, 14–19. [[CrossRef](#)]
96. Nandedkar, R.V.; Kesternich, W. Effect of boron on high-temperature creep behavior of austenitic stainless steel DIN 1.4970. *Metall. Trans. A* **1990**, *21*, 3033–3038. [[CrossRef](#)]
97. Fujiwara, M.; Uchida, H.; Ohta, S. Effect of boron and carbon on creep strength of cold-worked type 316 stainless steel. *J. Mater. Sci. Lett.* **1994**, *13*, 557–559. [[CrossRef](#)]

98. Mansfield, J.F. Identification of boron in M23X6 precipitates in 316 stainless steel using electron energy loss spectroscopy. *J. Mater. Sci.* **1987**, *22*, 1277–1285. [[CrossRef](#)]
99. Laha, K.; Kyono, J.; Sasaki, T.; Kishimoto, S.; Shinya, N. Improved creep strength and creep ductility of type 347 austenitic stainless steel through the self-healing effect of boron for creep cavitation. *Metall. Mater. Trans. A* **2005**, *36*, 399–409. [[CrossRef](#)]
100. Laha, K.; Kyono, J.; Kishimoto, S.; Shinya, N. Beneficial effect of B segregation on creep cavitation in a type 347 austenitic stainless steel. *Scripta Mater.* **2005**, *52*, 675–678. [[CrossRef](#)]
101. Laha, K.; Kyono, J.; Shinya, N. Some chemical and microstructural factors influencing creep cavitation resistance of austenitic stainless steels. *Philos. Mag.* **2007**, *87*, 2483–2505. [[CrossRef](#)]
102. Yao, X.X. On the grain boundary hardening in a B-bearing 304 austenitic stainless steel. *Mater. Sci. Eng. A* **1999**, *271*, 353–359. [[CrossRef](#)]

Disclaimer/Publisher’s Note: The statements, opinions and data contained in all publications are solely those of the individual author(s) and contributor(s) and not of MDPI and/or the editor(s). MDPI and/or the editor(s) disclaim responsibility for any injury to people or property resulting from any ideas, methods, instructions or products referred to in the content.